# Chapter 3

# Raman Scattering Characterization of Hexagonal GaN Layer on Sapphire Substrate

## 3.1 Introduction

In polar semiconductors, the free carrier plasma interacts with the longitudinal optical (LO) phonon via their macroscopic electric fields. As a results of this interaction, instead of a pure plasmon and a pure LO-phonon, Varga [1] proposed two coupled modes which have mixed phonon-plasmon characters for the first time. Raman scattering from LO-phonon-plasmon coupled modes in III–V semiconductors are extensively studied. The first observation of light scattering by photo excited LO-phonon-plasmon (LPP) coupled modes in III–V semiconductor was reported in GaP which was excited by the high-power pulsed dye laser [2]. Subsequently, extensive studies of light scattering by single-particle and collective excitations of the electron-hole plasma have been carried out, mainly on GaAs [3]. By contrast, very few studies have been reported so far on GaN. The first experiment on LPP coupled mode in GaN has been reported by using the infrared reflectivity and absorption measurements [4, 5]. This is because it has been difficult to grow high-quality GaN and undoped GaN films generally have a characteristic of $n$-type conductivity with a residual donor concentration of more than $10^{19}$ $cm^{-3}$ due to native defect or residual impurities. Recently, epitaxial films of GaN on sapphire substrates with high crystal quality and free-electron concentration of the $n$-type in the range from $1 \times 10^{16}$ to $1 \times 10^{19}$ $cm^{-3}$ by Si doping technology [6] have been reported. The development in the growth technique of GaN has been enabled one to characterize undoped and doped GaN by Raman spectroscopy.

In the heteroepitaxial GaN grown on sapphire substrate, there are two main problems: high mismatches of 1) lattice constants ($^{a}_{GaN} < {}^{a}_{Sapphire}$, $^{c}_{GaN} > {}^{c}_{Sapphire}$) and 2) thermal expansion coefficients ($\alpha$) between GaN film and substrate ($\alpha_{GaN} < \alpha_{Sapphire}$). These mismatches lead to large amount of interfacial biaxial compressive stress for GaN film at 300 K, which causes a high density of dislocations and associated threading defects. Thus, the performances of light emitted diodes (LEDs) and laser diodes (LDs) suffer from severe and deleterious effect. The problems caused by the lattice mismatch have been eliminated by using a GaN or an AlN buffer layer [7, 8, 9]. However, the thermal stress can hardly be avoided in a heteroepitaxial structures. Control of the residual stress constitutes an actual issue towards high performance of electrical or optical devices.

Optical spectroscopy techniques such as Raman scattering spectroscopy have long been recognized as extremely efficient methods to investigate compound semiconductor bulk as well as

heterostructures. This method is non-destructive way and requires no contact fabrication. Furthermore, it is applicable from micro to macro region by using a microscope. If phonons, which are straightforward signatures of bonds, are found to be well adapted probes they can be used to sample stress, interface morphology, free carrier concentration, mobility of free carrier, phase mixing, etc [10, 11, 12, 13]. Therefore, Raman scattering technique has bee a powerful tools for studying the electronic [14] and lattice dynamic properties [15] of semiconductor, and to characterize the crystalline quality of epitaxial layers.

In this chapter, the characteristics of $A_1$(LO)-phonon-plasmon coupled mode in $n$- and $p$-type GaN and the residual thermal stresses in post-growth patterned $n$-type GaN characterized by Micro–Raman scattering measurements will be discussed.

## 3.2 Experiments

Raman scattering measurements were performed using a JASCO NRS-2000 triple-grating spectrometer with a liquid nitrogen-cooled charge coupled device (CCD) array at 300 K. In most measurements, a 30 mW, 514.5 nm, argon ion ($Ar^+$) laser was used as the light source. A 50× ($N_A$ = 0.8) objective was employed, giving a laser illuminated spot of 1.5 to 2.5 $\mu$m in diameter, and resolutions were in the range from 0.1 $cm^{-1}$ to 1.0 $cm^{-1}$. The quasi-back-scattering geometry was employed.

A 2.4-$\mu$m-thick Si ($n$-type dopant) or Mg ($p$-type dopant) doped GaN film was grown via metalorganic chemical vapor deposition (MOCVD) at 1050°C on a 334 $\mu$m (0001) sapphire substrate with a 30-nm-thick GaN buffer layer deposited at 530°C. Trimethylgallium (TMG) was used as a group-III source, and ammonia ($NH_3$) was used as a group-V source. $SiH_4$ diluted in $H_2$ (10 ppm) was used as a $n$-type dopant. The carrier gas was hydrogen ($H_2$). No cracks were observed in both the epitaxial layer and substrate. The carrier concentration of films were determined by Van der Pauw Hall measurement at 300 K.

## 3.3 First-Order Raman Effect in Hexagonal Phase GaN

The primitive cell in the hexagonal structure contains twice as many as atoms as that of cubic. Since hexagonal structure belongs to the space group $C_{6\nu}^4$ ($P6_3mc$), a group theory analysis of $\mathbf{q} = 0$ lattice vibration predicts six optical modes. The full reducible representation may be decomposed into irreducible representations according to $\Gamma = A_1 + 2B_1 + E_1 + E_2$. The various optical phonon modes are illustrated in Fig. 3.1. The $E_2$ modes are Raman active, $A_1$ and $E_1$ modes are both Raman and infrared active and $B_1$ modes are silent, i.e, forbidden in Raman as well as infrared excitation modes. It is well known that an optical phonon, which is infrared active, will split into a LO and a transverse optical (TO) component due to the macroscopic electric field associated with the longitudinal vibration. As a results, $A_1$ and $E_1$ optical phonon modes are considerably influenced by macroscopic electric field. In the hexagonal structure, the phonons allowed in a backscattering geometry are given in Table 3.1, for the attainable polarization configurations on the two types of sample surface which are shown in Fig. 3.2.

Figure 3.3 shows typical Raman spectra from undoped GaN film grown on sapphire substrate at 300 K. From Van der Pauw Hall measurement, the film shows $n$-type conductivity and carrier concentration as $1.28 \times 10^{16}$ $cm^{-3}$ at 300 K. The phonon frequencies of all the observed modes are summarized in Table 3.2 and good agreement with the results of others. Some forbidden modes regarding to Raman selection rule are observed because the incident light is not exactly normal to the surface of the samples.

## 3.4 Mechanisms and Theory of Raman Scattering from Phonon-Plasmon Modes

### 3.4.1 Mechanisms

The Raman scattering from LO-phonon-plasmon coupled modes occurs by means of the following $A$ and $B$ terms:

$A$: modulation of the optical polarizability by the atomic displacements (deformation potential scattering) and by the microscopic longitudinal electric field (electro-optical scattering),

$B$: scattering due to density fluctuations of the free carriers.

The Raman efficiencies due to these mechanisms were deduced by several authors. The line shape of the coupled mode has been analyzed by the model developed by Hon and Faust, Klein *et al.* and Irmer *et al.* Klein *et al.* have indicated that the $A$ term in SiC and GaP is dominant compared with $B$ term. Irmer *et al.* have extended the treatment developed by Klein *et al.* to include the effect of phonon damping in Raman cross section. The Raman efficiency given by Irmer *et al.* consists of $A$ and $B$ terms. The $A$ term in cross section derived by Irmer *et al.* coincides with that obtained by Hon and Faust who have calculated the Raman shape of LO-phonon-plasmon modes regarding the crystal as a dielectric continuum.

### 3.4.2 Theoretical consideration

The Raman efficiency $I_A$ (due to $A$ term) due to the deformation-potential and electro-optic mechanisms is given by

$$\begin{aligned} I_A &= \frac{d^2A}{d\omega d\Omega}|_A \\ &= \frac{16\pi\hbar}{V_0^2}\frac{n2}{n1}\left(\frac{\omega_2}{c}\right)^4\left(\frac{\partial\alpha}{\partial E^L}\right)^2(n_\omega+1)\,AIm\left(-\frac{1}{\epsilon}\right), \end{aligned} \tag{3.1}$$

where

$$\begin{aligned} A = 1 &+ 2C\frac{\omega_T^2}{\Delta}\left[\omega_P^2\gamma(\omega_T^2-\omega^2)-\omega^2\Gamma(\omega^2+\gamma^2-\omega_P^2)\right] \\ &+ C^2\left[\frac{\omega_T^4}{\Delta(\omega_1^2-\omega_T^2)}\right]\left[\omega_P^2(\gamma(\omega_1^2-\omega_T^2)\right. \\ &+ \left.\Gamma(\omega_P^2-2\omega^2)+\omega^2\Gamma(\omega^2+\gamma^2))\right], \end{aligned} \tag{3.2}$$

and

$$\begin{aligned} \Delta = &\omega_P^2\gamma\left[(\omega_T^2-\omega^2)^2+(\omega\Gamma)^2\right] \\ &+ \omega^2\Gamma(\omega_L^2-\omega_T^2)(\omega^2+\gamma^2), \end{aligned} \tag{3.3}$$

where $\omega_T$ and $\omega_L$ are the TO and LO phonon frequencies, respectively, $\gamma$ is the plasmon damping constant, $\Gamma$ is the phonon damping constant, $\omega_1$ and $\omega_2$ are the incident and scattered photon frequencies, $V_0$ is the volume of the unit cell, $n_1$ and $n_2$ are the refractive indexes at $\omega_1$ and $\omega_2$ and $n_\omega$ is the Bose-Einstein factor. And $C$ is the Faust-Henry coefficient, which is determined by the intensity ratio between LO and TO phonons in the undoped GaN, which is given by

$$\frac{I_{LO}}{I_{TO}} = \left(\frac{\omega_1+\omega_L}{\omega_1+\omega_T}\right)^2\frac{\omega_T}{\omega_L}\left(1+\frac{\omega_T^2-\omega_L^2}{C\omega_T^2}\right). \tag{3.4}$$

The dielectric function $\epsilon$ is given in the presence of free carriers is given by

$$\epsilon = \epsilon_\infty\{1+\frac{\omega_L^2-\omega_T^2}{\omega_T^2-\omega^2+i\omega\Gamma}-\frac{\omega_P^2}{\omega(\omega+i\gamma)}\}, \tag{3.5}$$

where $\omega_P$ is the plasmon frequency

$$\omega_P^2 = \frac{4\pi n e^2}{\epsilon_\infty m^*}, \tag{3.6}$$

and $n$ is the free carrier concentration, $\varepsilon_\infty$ is the high frequency dielectric constant and $m^*$ is the effective mass.

Raman scattering method is based on detecting the changes in the frequency and linewidth of the longitudinal optical (LO) phonon spectra, which arise in the doped samples due to the interaction between the phonon and the plasma mode of the gas. From the analysis of the frequency shift and line shapes of the LO-phonon-plasmon modes by fitting $\omega_p$, $\gamma$, $\Gamma$ and $C$ in eq. (3.1), the concentration and mobility of the carriers can be determined.

## 3.5 Experimental Results and Discussion

### 3.5.1 $A_1$(LO) phonon-plasmon coupling in $n$-GaN

Two coupled modes ($\omega_+$, $\omega_-$) can be observed in GaAs or InP with high mobilities. According to the coupled-mode theory, the frequencies of two coupled LO-phonon-plasmon modes ($\omega_\pm$) in a doped polar semiconductor in the limit of long wavelength and with no phonon or plasmon damping are given by

$$\omega_\pm = \frac{1}{2}\left\{(\omega_{LO}^2 + \omega_P^2) + \left[(\omega_{LO}^2 + \omega_P^2)^2 - 4\omega_P^2\omega_{TO}^2\right]^{1/2}\right\}. \tag{3.7}$$

According to this, GaN with concentration of $1 \times 10^{17}$ cm$^{-3}$, taking $\omega_{\rm LO} = 736$ cm$^{-1}$, $\omega_{\rm TO} = 534$ cm$^{-1}$ and $m^* = 0.2 \cdot m_0$, eq. (3.7) gives $\omega_- = 67.9$ cm$^{-1}$ and $\omega_+ = 739$ cm$^{-1}$. However, plasmons are over-damped in GaN, SiC, II–VI compounds and GaP because of large collision damping [16]. For these films, the low-frequency branch of LO-phonon-plasmon coupled mode is not observed due to the broadness and the high-frequency branch shows a slight shift to the higher frequency side with the broadening of the LO mode as the carrier concentration is increased.

Figure 3.4 shows the frequency shifts of $E_2$ and $A_1$(LO) phonon modes. It should be noted that the frequency shift and line broadening of $E_2$ and $A_1$(LO) phonon modes have not observed with increasing an $Ar^+$ laser power up to 100 mW. Thus, the heating effect of the samples were neglected under the laser power of 30 mW used in this study. The frequency of the $E_2$ mode in all samples here did not vary ($568.2 \pm 0.2$ cm$^{-1}$) with the Hall carrier concentration. This indicates that $E_2$ phonon frequencies are independent of the carrier concentration. The frequency of $A_1$(LO) phonon mode increases slightly with increasing Hall carrier concentration below $10^{17}$ cm$^{-3}$, and increases rapidly above $3 \times 10^{17}$ cm $^{-3}$. The variation of the LO-phonon frequency with carrier concentration indicates that the LO-phonon mode is coupled with the over-damped plasmon in doped GaN crystals.

As mentioned in § 3.4.1, two main mechanisms ($A$ and $B$ terms) contribute to the Raman efficiency. However, the contribution of $A$ term (deformation potential scattering and electro-optic mechanisms) is larger compared to that of $B$ term (charge density fluctuation mechanism) in SiC [17] and GaP [18].

The $A_1$(LO) phonon spectra have been tried to fit the calculated line shape mentioned in § 3.4.2 to observe $A_1$(LO)-phonon-plasmon coupled mode by means of the least squares method. The Raman intensity of each $A_1$(LO) phonon spectra are normalized by the peak intensity. Prior to fit, the Faust-Henry coefficient $C$ was determined by using eq. (3.4). In this fitting, a fixed value of $C$ as 0.55 is used for all the samples. This $C$ value gives an asymmetric line shape. A rise of the low-frequency side of the $A_1$(LO)-phonon-plasmon coupled mode is very sensitive to $C$. Figure 3.5 shows typical line shapes of the experimental and the fitted spectra of the $A_1$(LO)-phonon-plasmon coupled mode. The theoretical fit is shown by the solid line. The agreement between the experimental and fitted line shapes is fairly good.

It should be noted that the line shape of fitted $A_1$(LO)-phonon-plasmon coupled mode became asymmetric and was worse if $B$ term (the density fluctuation mechanism) was included into $A$ term discussed § 3.4.1. Therefore, $A$ term was dominated in GaN like SiC or GaP.

Figure 3.6(a) shows the experimental and fitted $A_1$(LO)-phonon-plasmon coupled mode for several carrier concentrations measured by Van der Pauw Hall measurement at 300 K. All the samples were evaluated that the plasmon frequencies ($\omega_P$) were much smaller than the plasmon damping constants ($\gamma$) ($\omega_P \ll \gamma$). This result indicates that the plasmon in $n$-type GaN has large damping rates and the LO-phonon is coupled with the over-damped plasmon.

Using eq. (3.6), the free carrier concentration $n$ from the values of the plasmon frequency obtained by the line shape fitting where the values of the effective mass of electron ($m^*$) and the high-frequency dielectric constant ($\varepsilon_\infty$) were set to $0.2 \cdot m_0$ and 5.35, respectively.

In Fig. 3.6(b) the values obtained by Raman analysis are plotted against the carrier concentration deduced from Van der Pauw Hall measurements. It clear that the carrier concentrations obtained by Raman analysis are good agreement with those obtained by Hall measurement. Therefore, Raman method may be well established to determine the free carrier concentration of $n$-GaN.

The plasmon damping constants obtained by Raman analysis increase with increasing the concentration of carriers. The values of $\gamma$ are plotted in Fig. 3.7 as a function of those deduced from Hall measurement ($\gamma_H$) which is given by

$$\gamma_H = R_H \frac{e}{m^* \mu_H}, \tag{3.8}$$

where $\mu_H$ is the Hall mobility and $R_H$ is the Hall factor. In the calculation of $\gamma_H$, the acoustic phonon is assumed to be a dominant mechanism and then $R_H$ is equal to $3\pi/8$.

It seems that the plasmon damping constants obtained by Raman analysis did not coincide with the ones obtained by Hall measurements. Irmer *et al.* [19] reported deviation between the damping constants obtained by each method (Raman and Hall measurements) in GaP. They concluded this results in terms of the broadening effect of $A_1$(LO) phonon by doping rather than LO-phonon-plasmon coupling. Bairamov *et al.* [20] reported the line shape of the coupled mode in ZnO crystal dependent on the laser power at 77 K. They suggested that the creation of nonequilibrium carriers by the laser radiation is responsible for the difference between the values of damping constants deduced from Raman analysis and those from Hall measurement. As mentioned above, the laser power dependence of $A_1$(LO) phonon frequency shift has not observed in this study up to 100 mW. Thus, this explanation can not be applied to the results of this study. One of possible explanation of the relative larger deviation between the spectroscopical (Raman) and electrical (Hall) is the considered scattering mechanism. If the ionized impurity as well as the acoustic mechanisms contribute to the carrier scattering (add the impurity ionized scattering mechanism into eq. (3.8), the values of $\gamma_H$ may reduce. However, the detail mechanism is not clear at this time.

### 3.5.2 $A_1$(LO) phonon-plasmon coupling in $p$-GaN

For $p$-type GaN samples, the dopant as $Cp_2Mg$ was used. In general, hydrogen in a Mg-doped $p$-type GaN film forms a complex with Mg and electrically passivates the impurities. To realize $p$-type conductivity, a low energy electron beam irradiation (LEEBI) or thermal annealing is performed. In this experiments, the samples were annealed at 800°C for 30 minutes in a nitrogen environment to release hydrogen and obtain $p$-type conductivity.

Figures 3.7(a) and 3.7(b) show the Raman spectra of $p$-type and undoped samples in wide and low frequency ranges. There is no significant shift of $A_1$(LO)-phonon frequency in $p$-type GaN with increasing Mg doping concentration both with and without high temperature annealing treatments. The phonon frequencies from $p$-type GaN in the range from 400 to 900 $cm^{-1}$ are almost same as those obtained from undoped GaN except Raman intensities. This is strikingly different from that of $n$-type GaN as discussed earlier. However, from Fig. 3.7(b), there is a clear continuum band in Raman signal below 350 $cm^{-1}$ in $p$-type GaN. This continuum band is may be attributed to single-particle excitation of free carriers due to inter-valence-band transition as reported in heavily doped $p$-type Si [21]. Fano-interference effect appears when a sharp discrete transition overlaps with a continuum transition and interferences with it [22]. This interference

effect was weakly observed in the tail of the $E_2$ phonon band at 143 $cm^{-1}$. Looking at the detail of Raman signal around $E_2$ phonon mode, the asymmetric feature is observed and the spectral dip corresponding to anti-resonance appears at a higher frequency side. Harima *et al.* have observed that the symmetric feature becomes evident with increasing hole density and suggested that the Fano interference feature could be used as a measure of hole concentration [23]. At this time, there has not obtained the relationship between the Fano interference feature and Mg concentration clearly. Thus, it is difficult to conclude whether the hole concentration can be obtained from the Fano interference feature or not.

In order to reveal the reason why $A_1$(LO)-phonon frequency in $p$-type GaN does not change like $n$-type GaN, the theoretical calculations in terms of phonon damping constant ($\Gamma$), plasmon damping constant ($\gamma$) and carrier concentration (or plasmon frequency $\omega_P$) were performed. In the calculation, the simple form reduced from eq. (3.1) was used. The Raman efficiency $I_A$ is given

$$I_A \propto AIm\left(-\frac{1}{\varepsilon}\right), \tag{3.9}$$

with

$$A = \left[\frac{\omega_T^2(1+C)-\omega^2}{\omega_T^2-\omega^2}\right]^2, \tag{3.10}$$

where $C$ is Faust-Henry coefficient and $\varepsilon$ is given by eq. (3.5).

Figures 3.8(a), 3.8(b) and 3.8(c) show the results of calculation of LO-phonon-plasmon coupled mode under various plasmon damping conditions. The phonon damping constant $\Gamma$ was set to 20 $cm^{-1}$ and the carrier concentration were varied from $1 \times 10^{17}$ to $1 \times 10^{18}$ $cm^{-3}$ in the calculations. The $A_1$(LO) phonon shift were observed in both undamped ($\omega_P > \gamma$) and weakly damped ($\omega_P \leq \gamma$) conditions. In heavily damped ($\omega_P \ll \gamma$), however, the frequency shift was not observed. These calculated results indicate that the plasmon damping factor in $p$-type GaN is much larger than those in $n$-type GaN. Furthermore, the hole effective mass ($\simeq 0.8$) is heavier than that of electron effective mass ($= 0.19$). These effects strongly affect the $A_1$(LO)-phonon-plasmon coupled mode in $p$-type GaN.

## 3.6 Strain Relaxation in Post-Growth Patterned GaN Film

### 3.6.1 Sample preparation

In this section, the residual strain behavior of GaN film grown on a sapphire with various post-growth patterned squares fabricated by the focused ion beam (FIB) etching were studied by micro-Raman probing at 300 K. The growth conditions were mentioned in § 3.2. The carrier concentration of post-growth patterned GaN film as $n$ type of $1.28 \times 10^{17}$ $cm^{-3}$ was determined by Van der Pauw Hall measurement at 300 K. After growth, the sample was etched with the width of 2 $\mu$m to make the square $L$ varying from 5 $\mu$m to 100 $\mu$m fabricated by FIB etching. Top and cross-sectional images of post-growth patterned GaN are shown in Fig. 3.10.

### 3.6.2 Theoretical estimation of stress

Prior to experiment, the thermal stress in the as-grown GaN on sapphire was estimated by the model of Olsen and Ettenberg [24]. The theoretical and experimental investigations of the stress in the GaN on sapphire substrate have been reported by Hiramatsu *et al.* [25] and Kozawa *et al.* [26] In their reports, the same model (Olsen and Ettenberg [24]) was used assuming that the origin of the stress was due to only the difference in the thermal expansion coefficients between GaN and sapphire. This model is expressed in terms of Young's modulus $E_i$, thickness of film $t_i$ with length $L$ and width $W$, curvature $\kappa$, force $F_i$ and moment $M_i$, where $i = 1$ and 2 represent sapphire and GaN as shown in Fig. 3.11. In this study, the same methodology was used to

calculate the stress and curvature. When no external forces are applied, the forces and moments are in equilibrium:

$$\sum_{i=1}^{2} F_i = 0 \tag{3.11}$$

$$\sum_{i=1}^{2} \left[ \frac{E_i t_i L \kappa}{12} + F_i \left\{ \sum_{j=1}^{i} t_j - \frac{t_i}{2} \right\} \right] = 0. \tag{3.12}$$

The other equation is obtained by solving for the strain $\varepsilon$ at the interface between sapphire and GaN as

$$\varepsilon = \frac{F_2}{E_2 t_2 L} - \frac{F_1}{E_1 t_1 L} + \frac{(t_1 + t_2)\kappa}{2}. \tag{3.13}$$

The strain $\varepsilon$ is defined as $\varepsilon = \Delta T \cdot (\alpha_1 - \alpha_2)$, where $\alpha_1$ and $\alpha_2$ are the thermal expansion coefficients of sapphire and GaN, respectively and $\Delta T$ is the difference between growth temperature and room temperature. The stress distribution in the $i$-th layer $\sigma_i(z)$ is given by the sum of the stress due to the forces $F_i/t_i W$ and the bending stress $E_i \kappa(z - t_i/2)$, where $z$ is the position measure from the bottom of $i$-the layer. Assuming that $L \approx W$ and spherical bending, the two-dimensional stress can be estimated by one-dimensional stress as $\sigma_i(z)|_{2D} = \sigma_i(z)|_{1D}/(1 - \nu)$, where $\nu$ is the Poisson's ratio.

The parameters used in the calculation are listed in Table 3.4. The stress of 0.59 GPa and curvature of 0.13 $m^{-1}$ are obtained for the GaN film thickness $t_2$ of 2.4 $\mu$m which is the same as the sample studies here.

### 3.6.3 Experimental results and discussion

Figure 3.12 shows the $E_2$ phonon mode frequency and the full width at half maximum (FWHM) of $E_2$ mode phonon spectra as a function of $L$. The $E_2$ peak (at the center of the square) shift to the lower frequency, that is the relaxation of compressive stress in the plane of the layer, which is about 2 $cm^{-1}$ with decreasing the square size $L$. The estimated change of internal stress is about 6 kBar by using the biaxial stress coefficient of 2.9 $cm^{-1}$/GPa reported by Demangeot *et al.* [27].

They showed the phonon frequency as a function of biaxial stress that was calibrated by the 2 K reflectance study of energy difference between $A$ ($\Gamma_9$ valence band - $\Gamma_7$ conduction band) and $B$ ($\Gamma_7$ valence band - $\Gamma_7$ conduction band) excitons. The observed $E_2$ phonon frequency of as-grown sample in this study was similar to that of theirs. Thus the calculated stresses addressed in this study are highly reliable. It should be noted that the stress value of as-grown sample estimated here is good agreement with that estimated by the theoretical calculation discussed in § 3.6.2.

It is found that the internal stress changes drastically, below $L$=40 $\mu$m, as shown by the slopes of the dashed lines in Fig. 3.12(a). The $\Delta\omega$ of $E_2$ modes vary from 1.6 $cm^{-1}$ ($L$=5 $\mu$m) to 1.4 $cm^{-1}$ ($L$=100 $\mu$m) as a consequence of the change of the elastic constants with strain by the effect of post-growth patterning. The $\Delta\omega$ drastically decreases as increase in $L$ below $L$=40 and saturates at the value of as-grown.

Figures 3.13(a) and 3.13(b) show the mapping of $E_2$ phonon mode frequency measured by scanning the Raman probe in the direction as shown in the inset. In both results, the stress is almost zero at the edge of the pattern. But it increases drastically in several $\mu$m from the edge (the stress gradient is drastically changes in $\approx$ 10 $\mu$m) and then gradually approach to the equilibrium value in each $L$. Thus, the stress distribution is occurred in the square, that is, the peripheral and internal regions. The stress relaxation mechanism occurred at near edges is attributed to the expansion of the edges (edge facet is free to move) of layer by post-growth patterning [28].

The $A_1$(LO) phonon mode can couple with collective excitation of free carriers via longitudinal electric field and form LO-phonon-plasmon coupled mode as discussed in § 3.4.1, 3.4.2, 3.5.1

and 3.5.2. The spectral line shape of LO-phonon-plasmon modes changes sensitively with the doping concentration [29], however, the effect of internal stress is not clear till now. As seen in Fig. 3.14, the peak shift of $A_1$(LO) phonon measured at the center of each square is about 0.8 cm $^{-1}$ (736.8 - 737.6 cm $^{-1}$) which is much smaller than that of $E_2$ phonon mode. For the line width of $A_1$(LO) phonon as shown in Fig. 3.14(b), the variation of line width is much smaller than that of $E_2$ phonon mode. However, the change of linewidth in $A_1$(LO) phonon is same as that observed in $E_2$. Based on the biaxial stress coefficient as 0.8 cm$^{-1}$/GPa in ref. [27], the small change of $A_1$(LO) peak shift reflects the weak influence of the in-plane biaxial stress to the $A_1$(LO) phonon mode compared to $E_2$ mode. This is strongly attributed to the polarization, where $A_1$(LO) phonon is polarized in the $z$ direction and $E_2$ phonon is polarized in the $x-y$ plane as shown in Fig. 3.1. The spring constant (Ga-N) in the $x-y$ plane changes rather than those in the $z$ direction, especially at the edge facet, by the post-growth patterning. Thus, almost no shift is observed in $A_1$(LO) phonon by changing the square size $L$.

### 3.6.4 Stress reduction mechanism

Up to now, the stress reduction of GaN on sapphire substrate by using post-growth patterning method is discussed. The detail mechanism is not clear at this time, however, this may be due to the following mechanism.

The interface between GaN and sapphire substrate is rigidly connected even after post-growth patterning, however, the edge facet gradually moves outside ("edge moving effect") as it is away from interface to GaN top surface as shown in Fig. 3.15(a). Thus, the compressive stress at the interface remains relatively constant value. Furthermore, Fig. 3.12(a) indicates that the "edge moving effect" affects the residual stress at the center with square size $L \leq 40$ $\mu$m, however, it does not much affect at the center with square size $L \geq 40$ $\mu$m. The value $L = 40$ $\mu$m depends on the thickness of GaN layer.

The "edge moving effect" reduces the internal stress abruptly in several $\mu$m from the edge (peripheral region) and this effect is not much depend on the square size $L$ from Fig. 3.15(b).

## 3.7 Conclusions

In this chapter, the detailed discussion of $A_1$(LO)-phonon-plasmon coupled mode in various concentration of $n$ and $p$-type GaN on sapphire substrate and the residual thermal stresses in post-growth patterned $n$-type GaN on sapphire substrate characterized by Micro–Raman scattering technique at 300 K were presented.

In $n$-type GaN, $A_1$(LO)-phonon-plasmon coupled mode was observed and Raman spectra were performed line shape fitting based on the deformation potential scattering and electro-optical scattering mechanisms. The good agreement between the observed in this study and the theoretical fitted shapes was obtained. The free carrier concentrations and plasmon damping constants are determined and compared to those values obtained by Hall measurements. It is demonstrated that Raman measurement is a suitable technique to determine the free-carrier concentration. On the other hand, $p$-type GaN did not show $A_1$(LO)-phonon-plasmon coupled mode clearly. The theoretical calculation indicates that this characteristic is due to a over-damped plasmon damping factor (plasmon damping factor $\gg$ plasmon frequency) and an effective hole mass. A clear continuum band in the low-frequency region below $\approx 350$ cm$^{-1}$ was observed.

Reduction of the thermal stress in the post-growth patterned GaN on sapphire substrate was observed. The relaxation of compressive stress was observed with decreasing the square size $L$, especially in $\leq 40$ $\mu$m. The stress increased significantly within 10 $\mu$m away from edge, saturated. It was found that the internal stress was less important for the $A_1$(LO) phonon characteristic. These findings provide important hints for a device geometry.

Table 3.1: Selection rules of $q = 0$ Raman modes in GaN for various configurations used in the experiments. X, Y and Z are parallel to the $[01\bar{1}0]$, $[2\bar{1}\bar{1}0]$ and [0001] direction in the GaN film, respectively.

| Sample surface | Polarization configuration | Phonon |
|---|---|---|
| Face(0001) | $Z(Y\bar{Y})\bar{Z}$ | $A_1(LO), E_2$ |
| Edge | $X(Z\bar{Z})\bar{X}$ | $A_1(TO), E_2$ |
| | $X(Y\bar{Y})\bar{X}$ | $A_1(TO), E_1(LO)$ |

Table 3.2: Zone-center optical phonon frequencies in wrutzite GaN, in unit of $cm^{-1}$.

| Reference | $A_1$(TO) | $A_1$(LO) | $E_1$(TO) | $E_1$(LO) | $E_2$ |
|---|---|---|---|---|---|
| [30] | 533 | 735 | 561 | 743 | 569 |
| [31] | 533 | 735 | 561 | 742 | 570 |
| [32] | 534 | 736 | 563 | 746 | 572 |
| This work | 531 | 734 | 558 | 741 | 568 |

Table 3.3: Parameters used in $A_1$(LO) phonon-plasemon coupling characterizrion.

| Parameter | Notation | Optimized | Constant Value |
|---|---|---|---|
| $\omega_{1/2}$ | Incident and scattered phonon frequencies | | $\omega_1 = 19435$ cm$^{-1}$ |
| $n_{1/2}$ | Refractive indices of crystal at $\omega_{1/2}$ | | $n_1 = 2.3912$ |
| $\omega_{L/T}$ | LO-phonon and TO-phonon frequencies | | $\omega_T = 531$ cm$^{-1}$ |
| $\omega_P$ | Plasmon frequency | ○ | |
| $n_\omega$ | Bose-Einstein factor | | |
| $\gamma$ | Plasmon damping constant | ○ | |
| $\Gamma$ | Phonon damping constant | ○ | |
| $C$ | Faust-Henry coefficient | ○ | 0.55 (Optimized) |
| $E^L$ | Macroscopic electrical field | | |
| $\alpha$ | Polarizability | | |
| $n$ | Free-carrier concentration | | |
| $V_0$ | Volume of the unit cell | | |
| $m^*$ | Effective mass of the electron | | $0.20\mathrm{m}_0$ |
| $\epsilon_\infty$ | Dielectric constant | | 5.35 |

Table 3.4: Parameters used in the stress calculation.

| Parameters | | Sapphire ($i = 1$) | GaN ($i = 2$) |
|---|---|---|---|
| Thickness ($\mu$m) | $T_i$ | 300 | 2.4 |
| Young's modulas (GPa) | $E_i$ | 425 [33] | 196 [34] |
| Thermal expansion coefficient ($\times 10^{-6}$/deg) | $\alpha_i$ | 7.50 [25] | 5.45 [25] |
| Poisson ratio | $\nu_i$ | 0.3 | 0.3 |
| Temperature differnce (°C) | $\Delta_T$ | 1020 | |

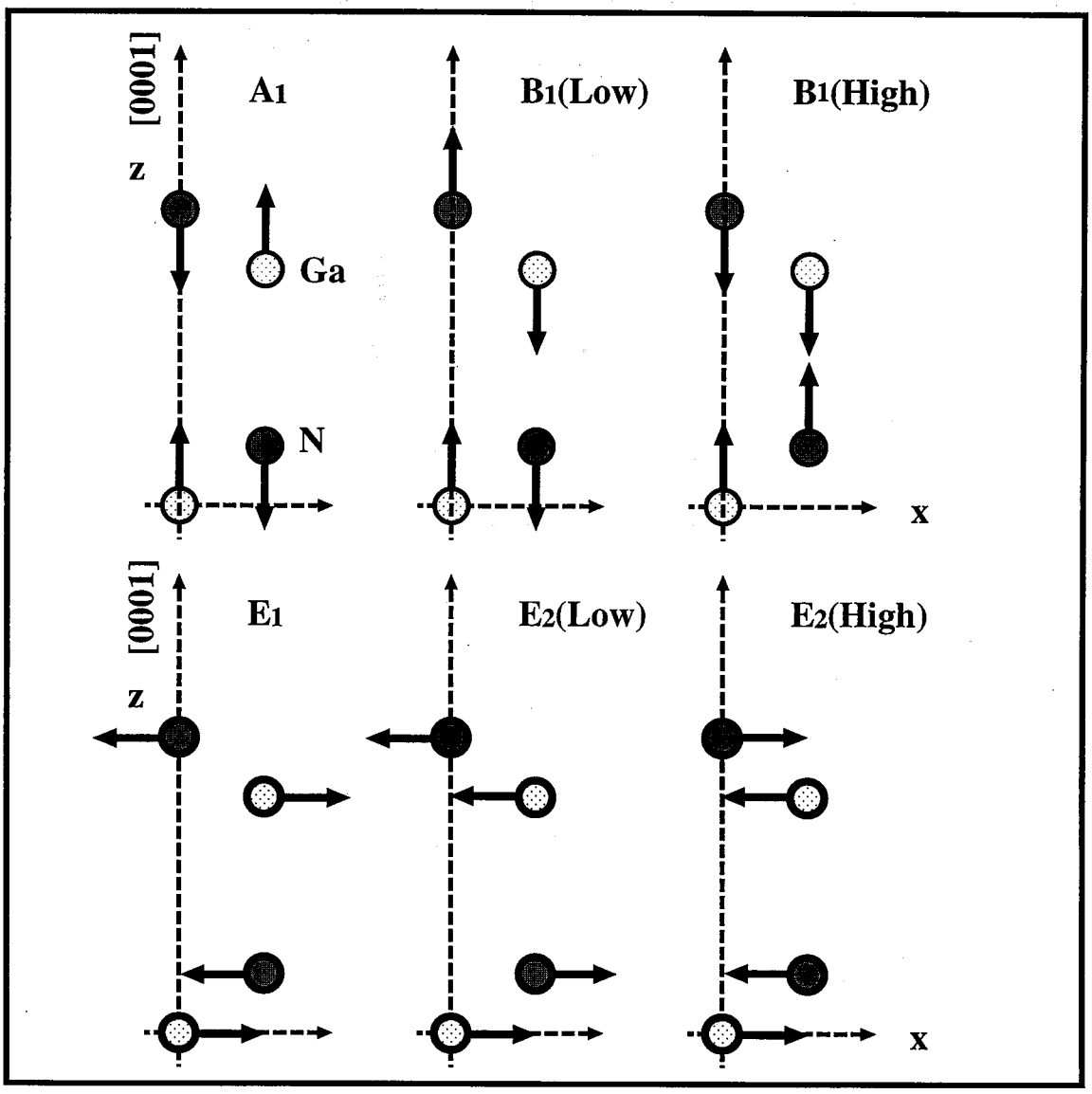


Figure 3.1: Optical phonon modes in the hexagonal GaN structure.

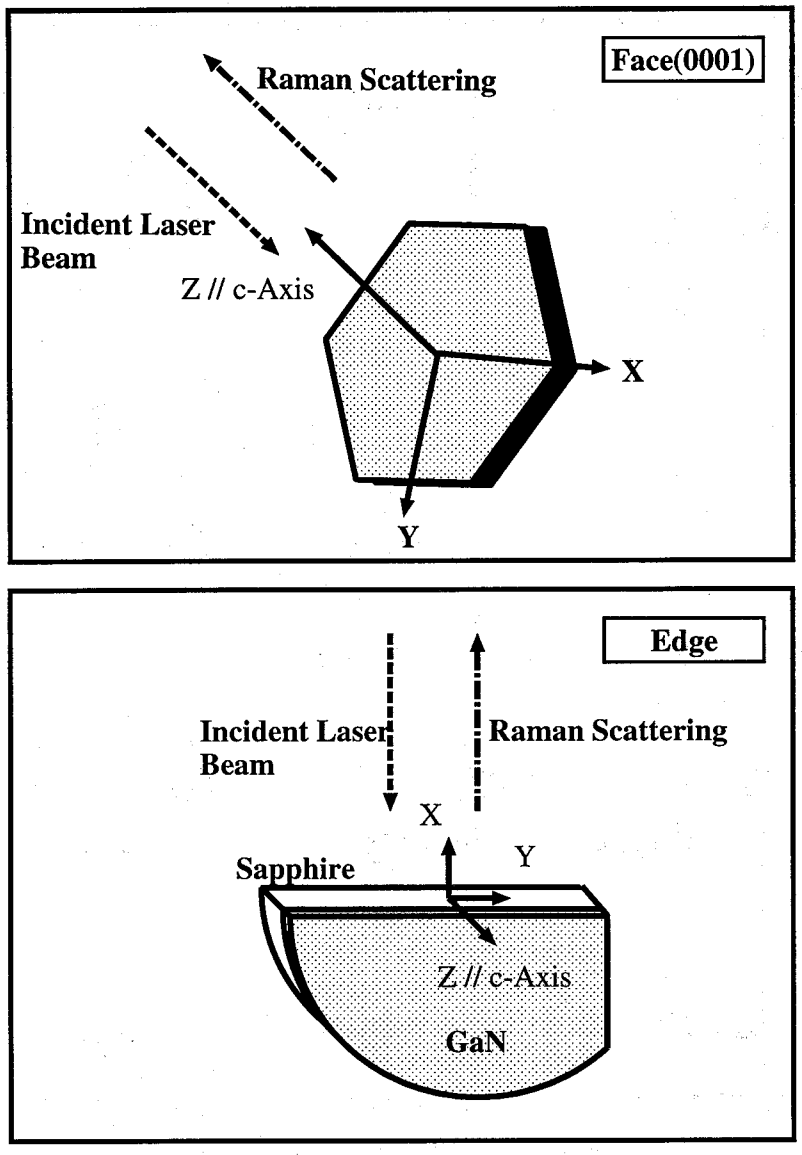


Figure 3.2: Raman scattering measurements were performed in backscattering geometry with $X(Z-)\bar{X}$, $X(Y-)\bar{X}$ and $Z(Y-)\bar{Z}$ configurations.

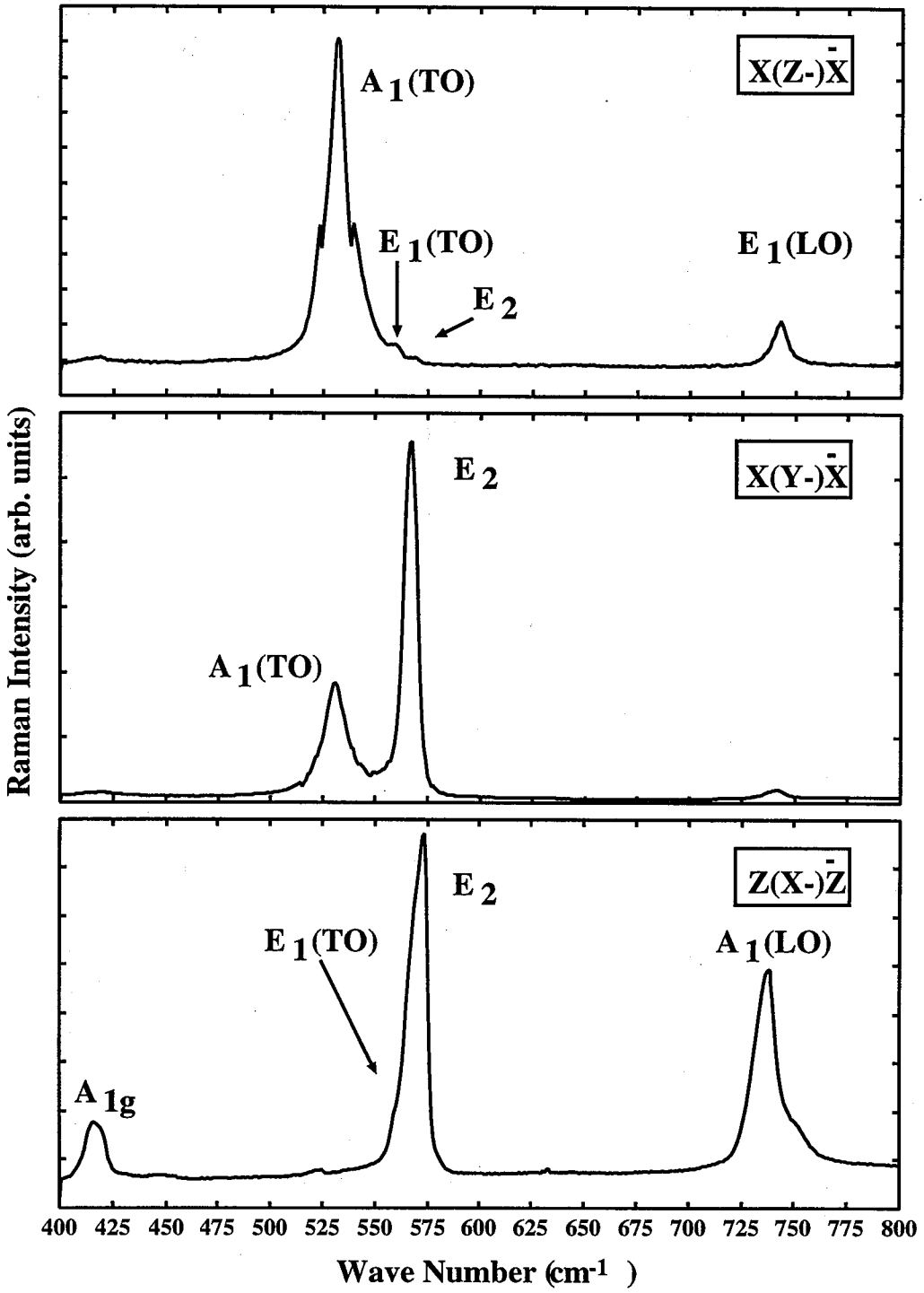


Figure 3.3: Typical Raman spectra of undoped GaN epitaxial layer at 300 K. The spectral resolution was 1 $cm^{-1}$.

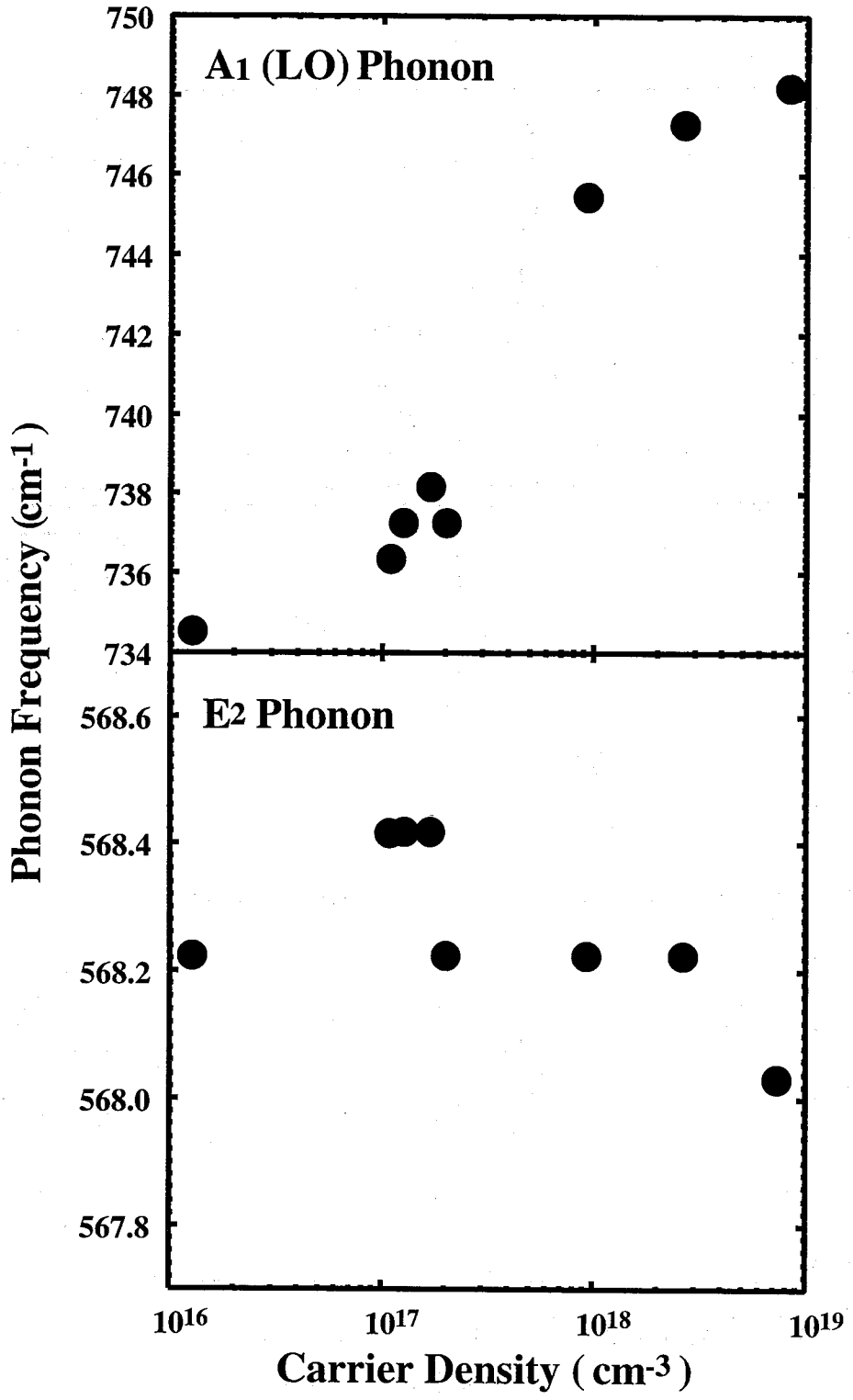


Figure 3.4: The peak positions of $E_2$ and $A_1$(LO) plasmon modes are plotted as a function of the carrier concentration.

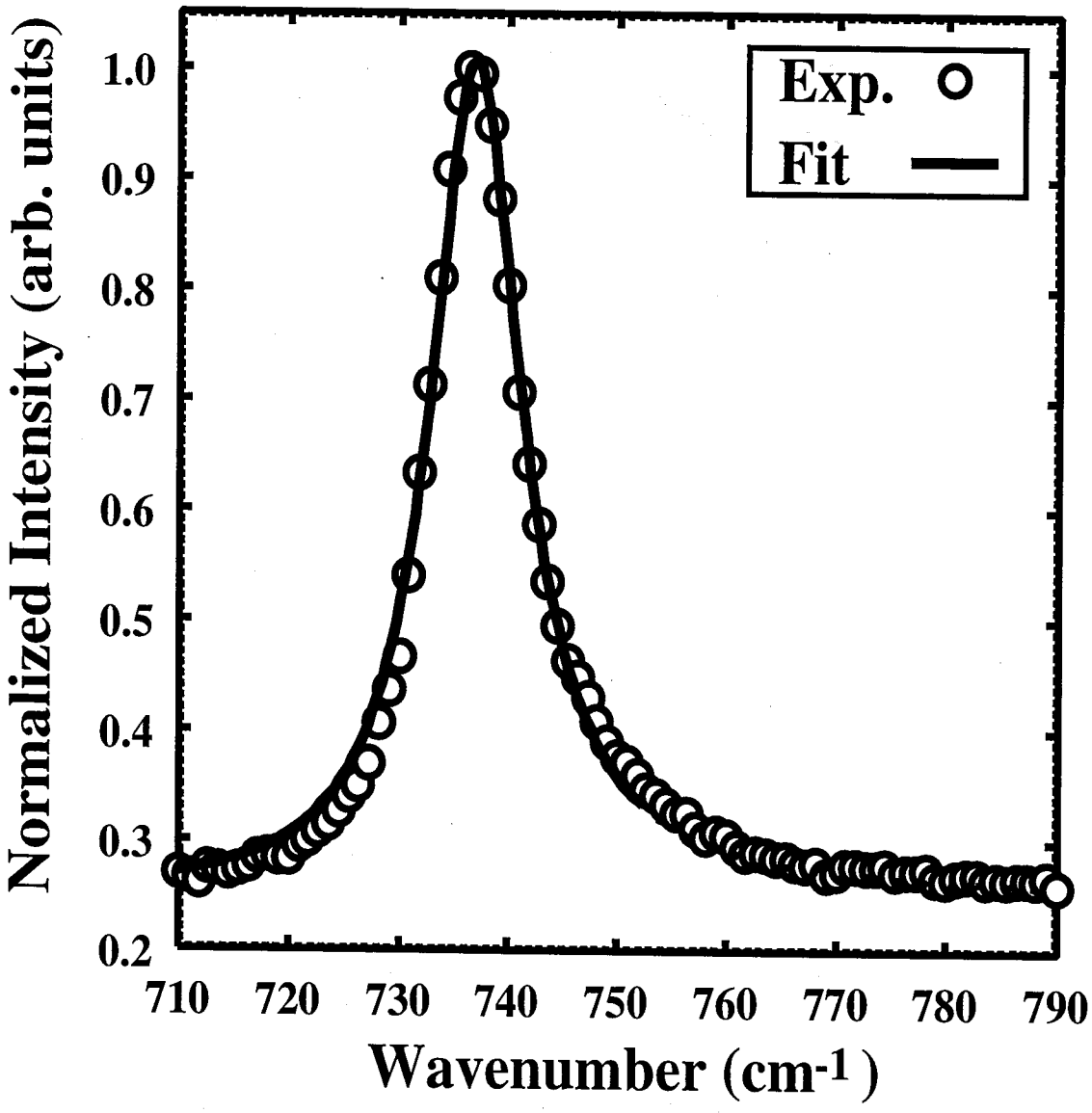


Figure 3.5: Comparison of the experimental and calculated Raman lines shapes of the $A_1$(LO)-phonon-plasmon coupled mode.

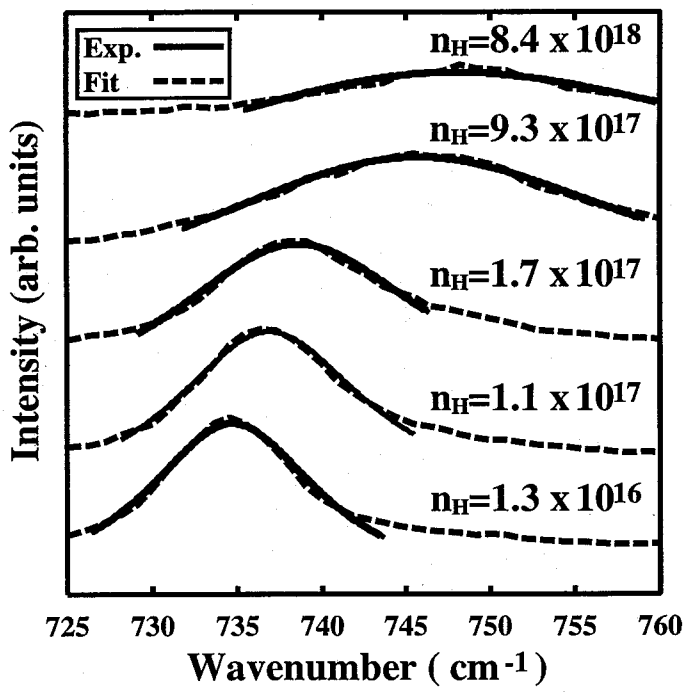


(a) Results of fitted $A_1$(LO) phonon Raman spectra compared with experimental results.

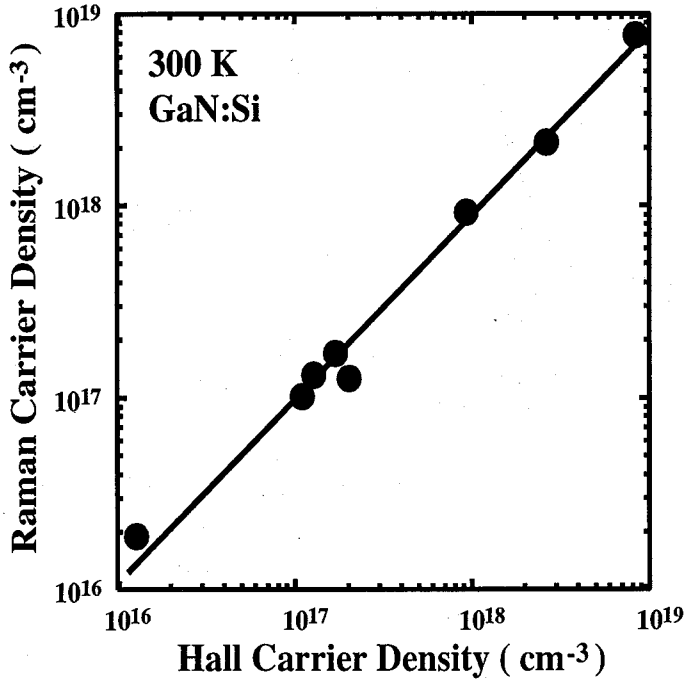


(b) The free-electron concentrations obtained from Raman measurements compared with those from Hall measurements.

Figure 3.6: Analysis of $A_1$(LO) phonon-plasmon coupled mode.

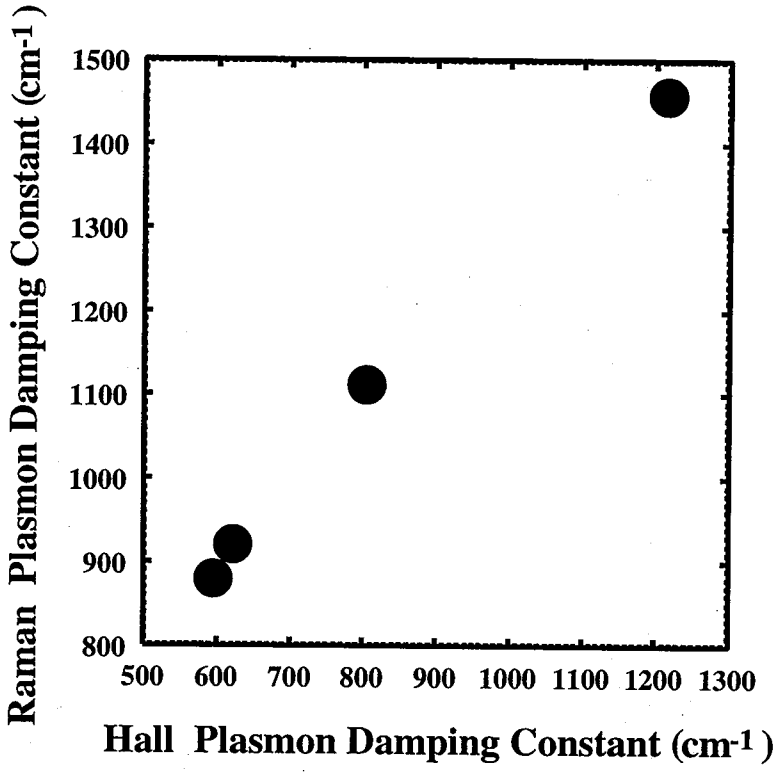


Figure 3.7: The plasmon damping constant $\gamma$ calculated from the Raman scattering measurement data versus those obtained from the Hall measurement data.

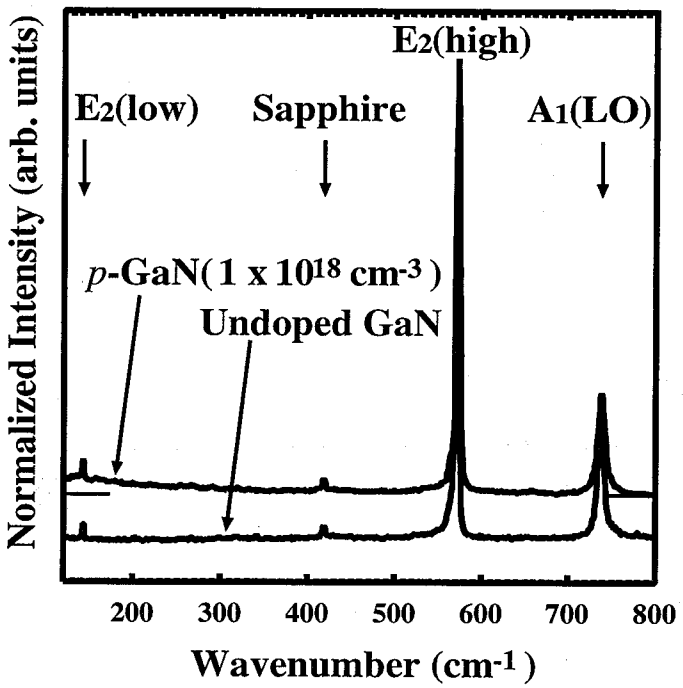


(a) Wide range frequency spectra of $p$ and undoped GaN. Spectra are shifted arbitrarily along the originate for comparison.

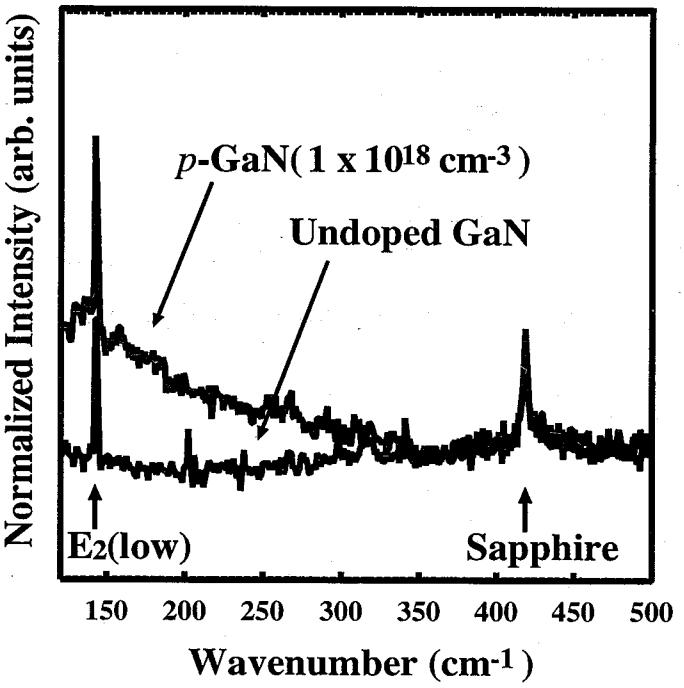


(b) Low frequency spectra of $p$ and undoped GaN. The spectra are plotted without shifting along the originate.

Figure 3.8: Raman spectra of $p$ and undoped GaN.

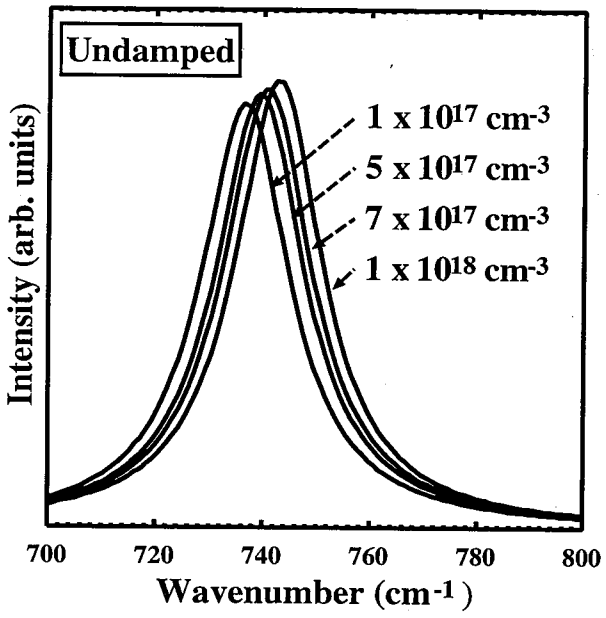


(a) Simulated for undamped condition ($\omega_P > \gamma$).

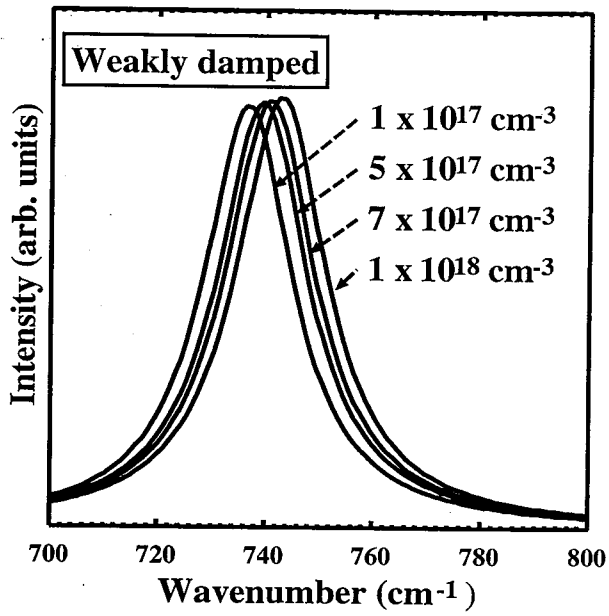


(b) Simulated for weakly damped condition ($\omega_P \leq \gamma$).

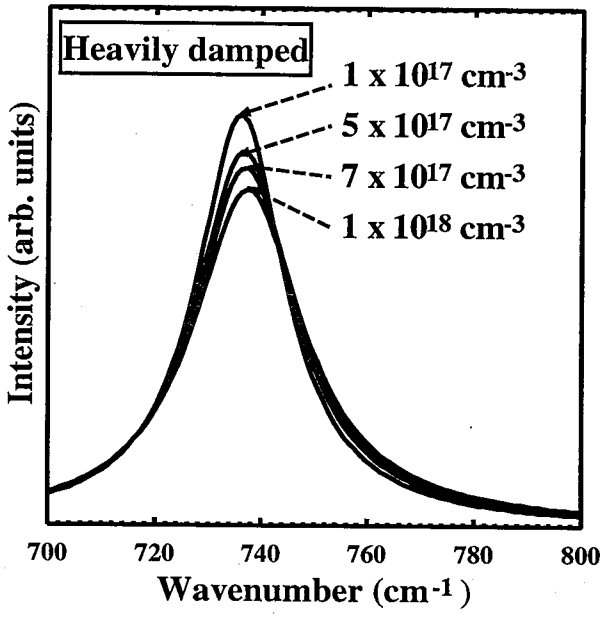


(c) Simulated for heavily damped condition ($\omega_P \ll \gamma$).

Figure 3.9: Simulated $A_1$(LO) phonon-plasmon coupled modes in $p$-type GaN.

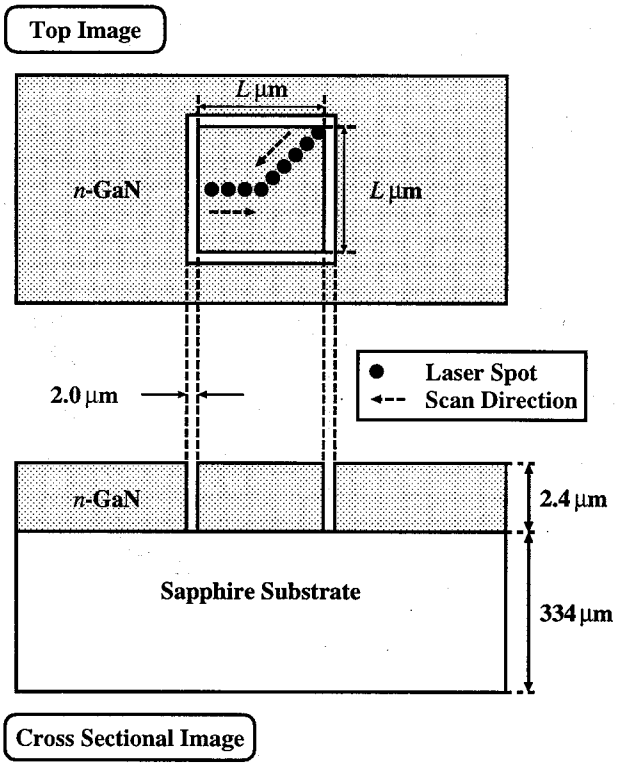


Figure 3.10: Top and cross sectional images of post-growth patterned GaN sample.

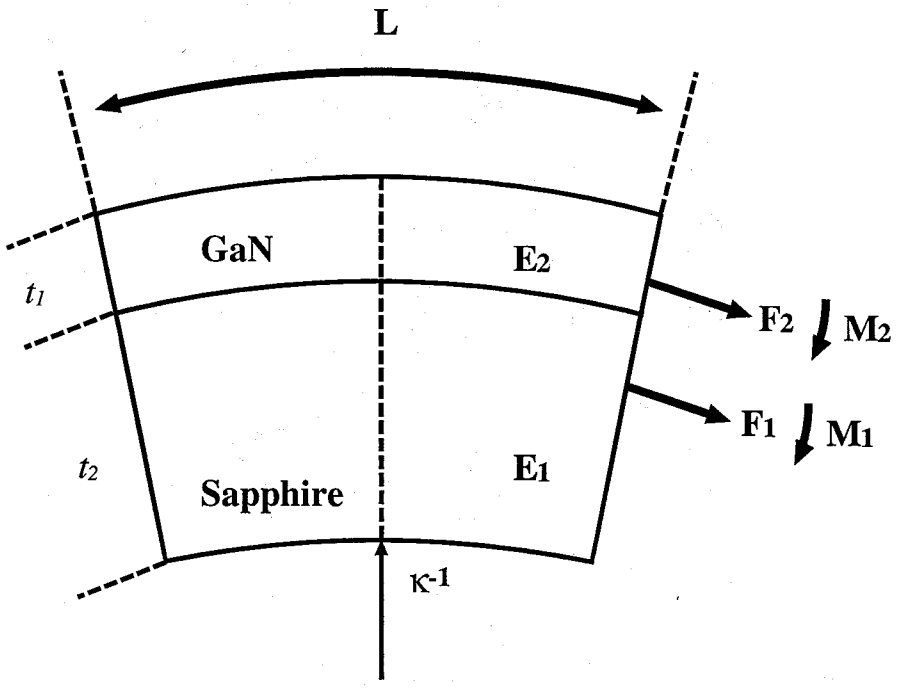


Figure 3.11: Schematic cross-sectional view of GaN/sapphire used the stress calculation.

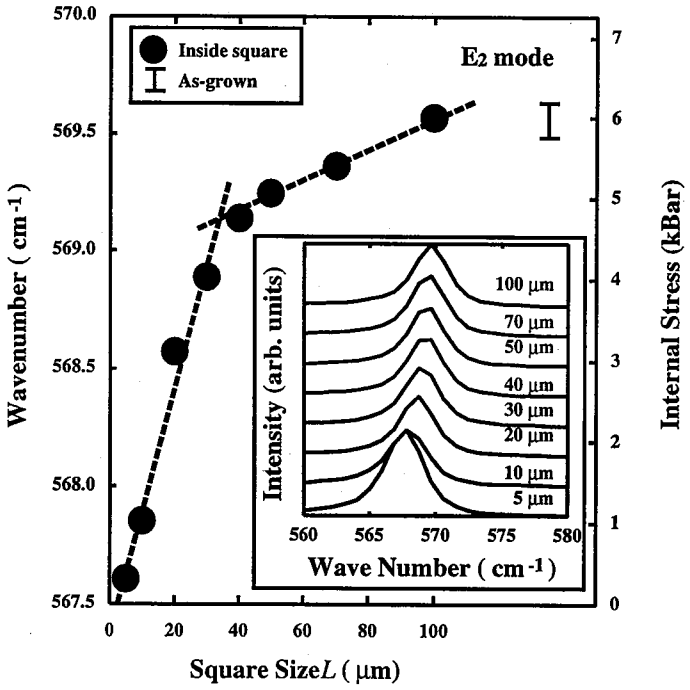


(a) $E_2$ mode frequency as a function of square size $L$.

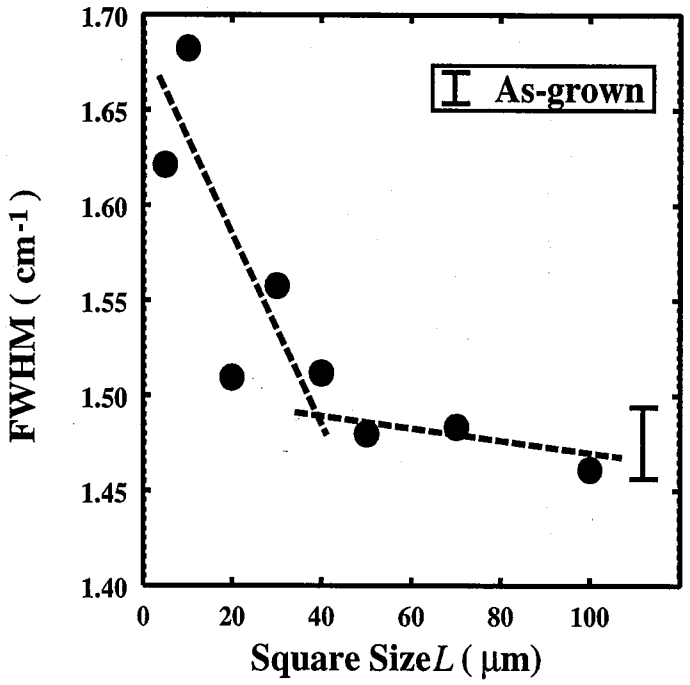


(b) FWHM of $E_2$ mode frequency as a function of square $L$.

Figure 3.12: $E_2$ phonon mode characteristics as a function of square size $L$.

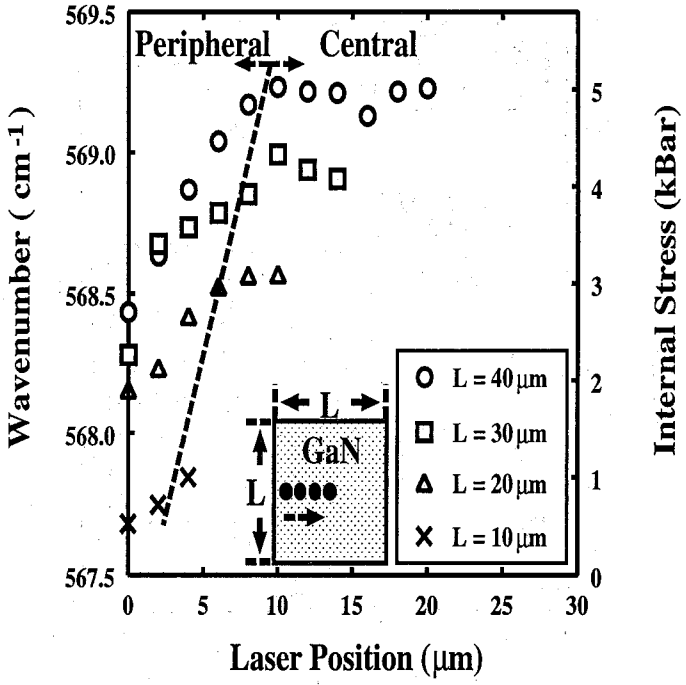


(a) Mapping of $E_2$ mode frequency.

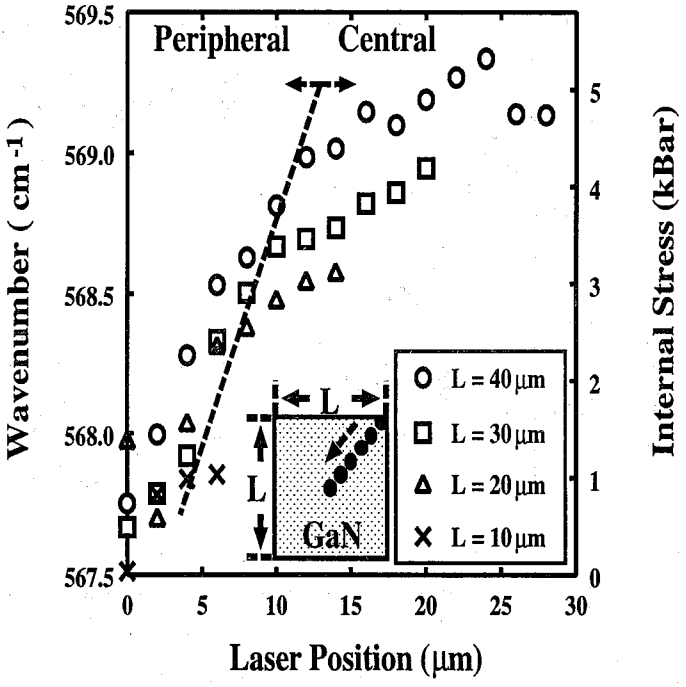


(b) Mapping of $E_2$ mode frequency in diagonal direction.

Figure 3.13: Mapping of $E_2$ phonon mode frequency.

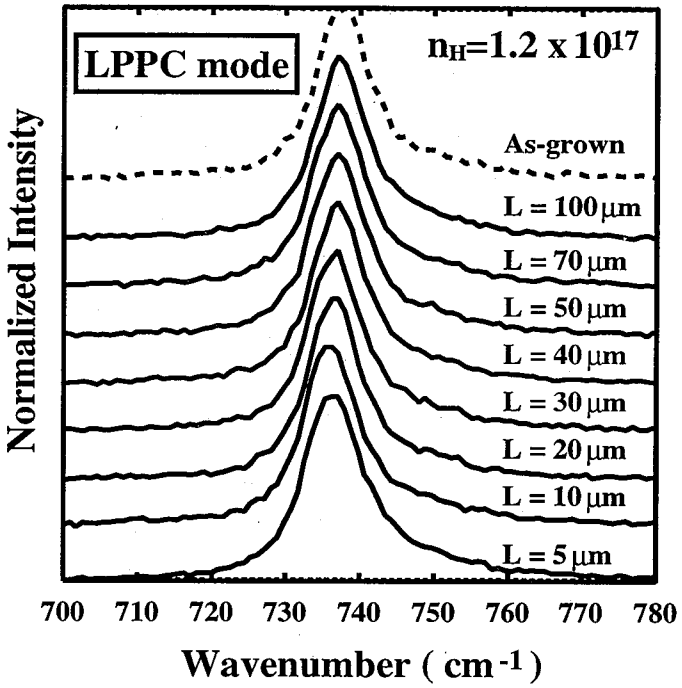


(a) $A_1$(LO) mode frequency as a function of square size $L$.

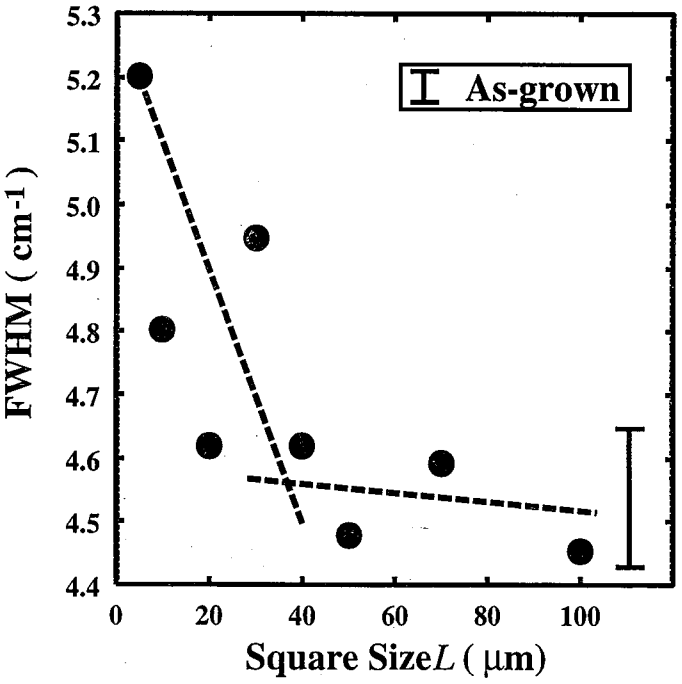


(b) FWHM of $A_1$(LO) mode frequency as a function of square size $L$.

Figure 3.14: $A_1$(LO) phonon mode characteristics as a function of square size $L$.

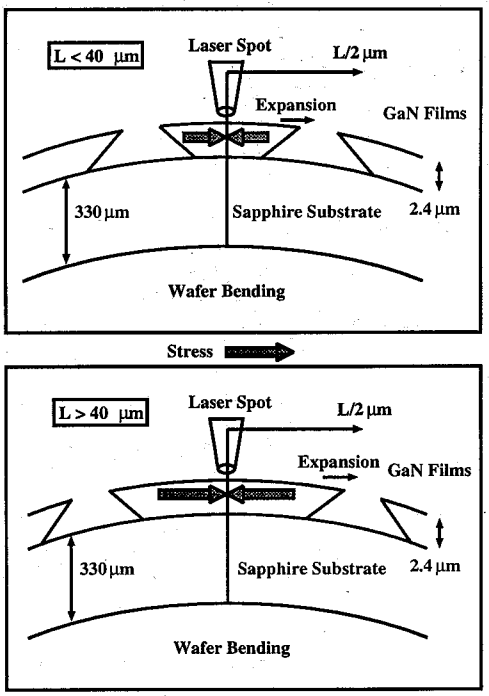


(a) Stress around square size $L$=40 $\mu$m.

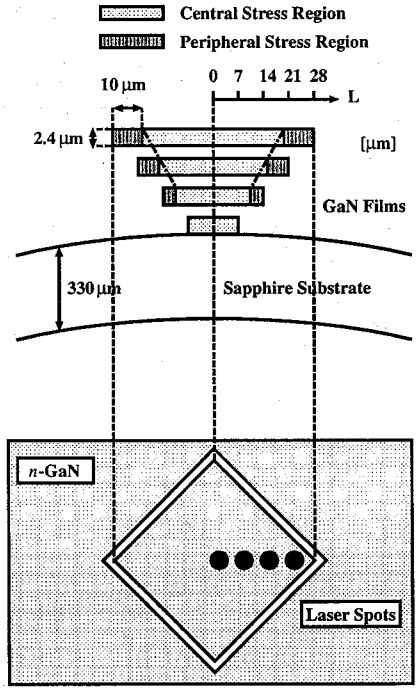


(b) Stress at peripheral and central regions in square size $L$.

Figure 3.15: Stress relaxation mechanism and stress distribution in post-growth patterned $n$-type GaN.

# Bibliography


[1] B. B. Varga: Phys. Rev. **137** (1965) A1896.

[2] J. E. Kardontchik and E. Cohen: Phys. Rev. Lett. **42** (1979) 669.

[3] G. Abstreiter, M. Cardona and A. Pinczuk, in *Light Scattering in Solid IV*, edited by M. Cardona and G. Gŭntherodt, Topics in Applied Physics Vol. 54 (Springer-Verlag, Berlin, 1984).

[4] A. S. Barker, Jr. and M. Ilegems: Phys. Rev. B **7** (1973) 743.

[5] R. Ruppin and J. Nahum: J. Phys. Chem. Solids **35** (1974) 1131.

[6] N. Koide, H. Kato, M. Sassa, S. Yamasaki, K. Manabe, M. Hashimoto, H. Amano, K. Hiramatsu and I. Akasaki: J. Cryst. Growth **115** (1991) 639.

[7] H. Amano, N. Sawaki, I. Akasaki and Y. Toyoda: Appl. Phys. Lett. **48** (1986) 353.

[8] I. Akasaki, H. Amano, Y. Koide, K. Hiramatsu and N. Sawaki: J. Cryst. Growth **98** (1989) 209.

[9] S. Nakamura: Jpn. Appl. Phys. **30** (1991) L1705.

[10] G. Attolini, L. Francesio, P. Franzosi and C. Pelosi: J. Appl. Phys. **75** (1994) 4156.

[11] H. Tanino, A. Amano. H. Kawanami and H. Matsuhata: J. Appl. Phys. **70** (1991) 7068.

[12] P. Wickboldt, E. Anastassakis, K. Sauer and M. Cardona: Phys. Rev. B **35** (1987) 1362.

[13] F. Cerderia, C. J. Buchenauer, F. H. Pollak and M. Cardona: Phys. Rev. B **5** (1972) 580.

[14] P. Manuel, G. A. Sai-Halasz, L. L. Chang, C. -A. Chang and L. Esaki: Phys. Rev. Lett. **37** (1976) 1701.

[15] B. Jusserand, D. Paquet, A. Regreny and J. Kerrarec: Solid State Commun. **48** (1983) 499.

[16] Y. Yugami, S. Nakashima, A. Mitsuishi, A. Umemoto, M. Shigeta, K. Furukawa, A. Suzuki and S. Nakajima: J. Appl. Phys. **61**, 354 (1987).

[17] M. V. Klein, B. N. Ganguly and P. J. Colwell: Phys. Rev. B **6** (1972) 2380

[18] D. T. Hon and W. L. Faust: Appl. Phys. **1** (1973) 241.

[19] G. Irmer, V. V. Toporov B. H. Bairamov and J. Monecke: Phys. Status Solidi B **119** (1983) 595.

[20] B. H. Bairamov, A. Heinrich, G. Irmer, V. V. Toporov and E. Ziegler: Phys. Status Solidi B **119** (1983) 227.

[21] F. Cerdeira, T. A. Fjeldly and M. Cardona: Phys. Rev. B **8** (1973) 4734.

[22] U. Fano: Phys. Rev. **124** (1961) 1866.

[23] H. Harima, H. Sakashita, T. Inoue and S. Nakashima: *Proc. of The Second International Conference on Nitrides Semiconductors*, Oct. 27-31 (1997), Tokushima, Japan.

[24] G. H. Olsen and M. Ettenberg: J. Appl. Phys. **48** (1977) 2543.

[25] K. Hiramatsu, T. Detchprohm and I. Akasaki: Jpn. J. Appl. Phys. **32** (1993) 1528.

[26] T. Kozawa, T. Kachi, H. Nagase, N. Koide and K. Manabe: J. Appl. Phys. **75** (1995) 4389.

[27] F. Demangeot, J. Frandon, M. A. Renucci, O. Briot, B. Gil and R. L. Aulombard: Solid State Commun. **100**, 207 (1996).

[28] J. W. Ager III, G. Conti, L. T. Romano and C. Kisielowski: Mater. Res. Soc. Symp. Proc. **482**, 769 (1998).

[29] T. Kozawa, T. Kachi, H. Kano, Y. Taga, M. Hashimoto, N. Koide and K. Manabe: J. Appl. Phys. **75**, 1098 (1994).

[30] T. Azuhata, T. Sota, S. Suzuki and S. Nakamura: J. Phys.: Condens. Matter **7** (1995) L129.

[31] H. Siegle, L. Eckey, M. Hoffmann, C. Thomsen, B. K. Meyer, D. Schikora, M. Hankeln and K. Lischka: Solid State Commun. **96** (1995) 943.

[32] T. Kozawa, T. Kachi, H. Kano, Y. Taga and M. Hashimoto: J. Appl. Phys. **75** (1994) 1098.

[33] J. B. Wachtman, Jr., W. E. Tefft, D. G. Lam, Jr. and R. P. Stinchfield: J. Res. Nat. Bur. Stand. **64A** (1960) 213.

[34] V. A. Savastenko and A. U. Sheleg: Status Solidi A **48** (1978) K135.